Hysteretic performance of stainless steel double extended end-plate beam-to-column joints subject to cyclic loading

Gao, J. D.; Du, X. X.; Yuan, H. X.; Theofanous, M.

DOI:
10.1016/j.tws.2021.107787

Document Version
Peer reviewed version

Citation for published version (Harvard):
Gao, JD, Du, XX, Yuan, HX & Theofanous, M 2021, 'Hysteretic performance of stainless steel double extended end-plate beam-to-column joints subject to cyclic loading', *Thin-Walled Structures*, vol. 164, 107787. https://doi.org/10.1016/j.tws.2021.107787

Hysteretic performance of stainless steel double extended end-plate beam-to-column joints subject to cyclic loading

J.D. Gao[a], X.X. Du [a,*], H.X. Yuan[a,*], M. Theofanous[b]

[a] *Hubei Provincial Key Laboratory of Safety for Geotechnical and Structural Engineering, School of Civil Engineering, Wuhan University, Wuhan 430072, PR China*

[b] *Department of Civil Engineering, University of Birmingham, Birmingham B15 2TT, United Kingdom*

Corresponding author:

Prof. Xinxi Du, School of Civil Engineering, Wuhan University, Wuhan 430072, China. Email: duxinxi@163.com

Dr Huanxin Yuan, School of Civil Engineering, Wuhan University, Wuhan 430072, China. Email: yuanhx@whu.edu.cn

Abstract: This paper focuses on the hysteretic performance of stainless steel beam-to-column joints with double extended end-plate connections under cyclic loading. Six full-scale joint specimens were fabricated, including three interior column joints and three exterior column joints. Two stainless steel grades – austenitic grade EN 1.4301 and duplex grade EN 1.4462, and one carbon steel grade Q345B were considered. A4-80 stainless steel bolts and grade 10.9 high strength steel bolts were employed to assemble the joint specimens. The cyclic loading tests were conducted using the loading protocol set in Chinese standard JGJ/T 101. The force versus displacement (F-Δ) hysteresis curves were recorded, and the failure modes, the ductility, the strength and stiffness degradation, and the energy dissipation capacity of the tested joints were analysed and discussed in detail. Empirical hysteresis models were developed and calibrated against the recorded hysteretic curves and energy dissipation capacities of the tested joints. The experimental results involving the initial rotational stiffness values and the moment resistances were further utilised to evaluate the accuracy of current design provisions codified in EN 1993-1-8, ANSI/AISC 358 and GB 51022. The comparison shows that the development of accurate design guidance accounting for the pronounced strain hardening of stainless steels is warranted.

Key words: Stainless steel; Beam-to-column joint; End-plate connection; Hysteretic performance; Experimental test; Design method; Cyclic loading; Ductility; Failure

1 Introduction

Beam-to-column joints with bolted end-plate connections can provide desirable attributes for seismic design due to their favourable hysteretic behaviour [1]. Unlike the more commonly used pinned connections and rigid connections [2], bolted end-plate connections usually exhibit semi-rigid behaviour. The hysteretic performance, yield mechanism and failure modes of carbon steel beam-to-column joints subject to cyclic loading have been investigated experimentally [3-5], whilst analytical and numerical investigations have also been reported in [6-8]. It has been demonstrated that stiffened end-plate connections can be employed in moment resisting frames as they possess sufficient strength, stiffness, ductility and energy dissipation capacity provided that bolt fracture is prevented by ensuring that failure of other more ductile components precedes bolt fracture [9,10].

The structural applications of stainless steels have been significantly extended in recent years due to the inherent excellent corrosion resistance and improved understanding of the life cycle cost. Meanwhile, the impact of the material non-linearity characteristics of stainless steels that differ considerably from ordinary carbon steels has received much attention from researchers. Elflah et al. [11-13] conducted a series of experimental tests on twelve single-sided austenitic stainless steel beam-to-column joints, including four types of configurations: flush and extended end-plate connections, top and seat angle cleat connections, and top, seat and double web cleat connections, which were further utilised to verify the developed FE models. Yuan et al. [14-16] completed forty tests on the key component of joints –

T-stubs in tension made of austenitic and duplex grades, and proposed a revised formula for predicting the plastic resistance. Hasan et al. [17,18] studied the monotonic behaviour of austenitic stainless steel top-seat angle bolted connections and top-seat double web angle connections. Eladly [19] proposed a simplified three dimensional (3D) FE model, which was validated against the experimental results reported in Ref. [11]. Gao et al. [20,21] completed six full scale tests on double extended end-plate beam-to-column joints made of carbon steel and stainless steel grades, and explored the influences of key parameters by numerical simulation. However, significantly fewer studies have been reported on the hysteretic behaviour of stainless steel beam-to-column joints subjected to cyclic loading. Wang et al. [22] tested five austenitic stainless steel beam-to-column joints with welded flange and bolted web connections subjected to cyclic loading. Liu and Shi [23] carried out cyclic tests on three duplex stainless steel beam-to-column joints with welded unreinforced flange-welded web connections, while Bu et al. [24] reported experimental results of five austenitic stainless steel bolted extended end-plate beam-to-column joints under cyclic loading. Besides, Yuan et al. [25] conducted a series of cyclic tests on stainless steel T-stubs and proposed a novel hysteretic model. It can be found that the cyclic loading tests on stainless steel beam-to-column joints were presented by the current studies, while the comparison of hysteretic performance between stainless steel end-plate beam-to-column joints and carbon steel counterparts as well as the difference of beam-to-interior column joints and exterior counterparts is still needed to be conducted, which is the focus of this study.

A total of six full scale end-plate beam-to-column joint specimens were fabricated and tested under cyclic loading, including one carbon steel benchmark specimen and five stainless steel specimens. The hysteretic performance of the tested joints, as well as key results including the load-carrying capacity, the failure modes, the degradation of strength and stiffness, the ductility capacity and the energy dissipation capacity are reported and discussed in detail. The obtained experimental results were utilised to develop an empirical model, that predicts the hysteresis curves and the cumulatively dissipated energy, and they were further utilised to assess the applicability of design provisions in three existing design codes, including EN 1993-1-8 [26], ANSI/AISC 358 [27] and GB 51022 [28]. It is envisaged that this experimental study will also provide a research database for the ongoing revision of the Chinese design standard for stainless steel structures [29].

2 Experimental programme

2.1 Description of joint specimen

A total of six full-scale double extended end-plate beam-to-column joint specimens were fabricated from hot-rolled plates, with three of the specimens being beam-to-interior column joints and three beam-to-exterior column joints. The configuration details of each specimen are summarised in Table 1. Five of the specimens were made of two stainless steel grades – austenitic grade EN 1.4301 (ASTM 304, GB S30408) and duplex grade EN 1.4462 (ASTM 2205, GB S22253), whilst the remaining beam-to-interior column joint was made of carbon steel grade Q345B and was used as a benchmark specimen against which the performance of similar stainless steel specimens was compared. The labelling convention for each joint specimen indicates the material grade, the joint type and the presence or absence of rib stiffeners. For example, specimen 'S22253-ISC-r' indicates a beam-to-interior column joint made of grade EN 1.4462 stainless steel with triangular rib stiffeners. Except for the specimen S30408-ESC, the end-plates of all other specimens are reinforced with 6 mm thick triangular rib stiffeners.

Austenitic stainless steel bolts in grade A4-80 were used to assemble the three austenitic stainless steel joints, while high strength bolts in grade 10.9 were employed for the carbon steel joint and the two duplex stainless steel joints. The designed pretension forces of bolts (F_{pre}) are tabulated in Table 1, which were carefully implemented by monitoring the tightening process. The design pretension forces for both grade A4-80 and grade 10.9 bolts were taken as 124 kN and 155 kN, respectively, by referring to EN 1993-1-8 [26]. In addition, the axial force (F_c) applied to the column was

taken as 20% of the cross-sectional yield resistance, as listed in Table 1, which remained constant throughout the cyclic loading process. The six specimens tested under cyclic loading are identical in terms of geometric configuration, employed material, applied bolt pretension and applied column load to the ones tested in [21] under monotonic loading, thus allowing a direct comparison of the results and the static force-deflection curve to be utilised as an envelope curve of the cyclic response.

Table 1

Configuration details of joint specimens

Specimen	Material grade	Bolt grade	Bolt pretension force F_{pre} (kN)	Column axial force F_c (kN)	End-plate rib stiffener	Joint type
Q345B-ISC-r	Q345B	10.9	155	375	Yes	
S30408-ISC-r	EN 1.4301	A4-80	124	290	Yes	Beam-to-interior column joint
S22253-ISC-r	EN 1.4462	10.9	155	565	Yes	
S30408-ESC-r	EN 1.4301	A4-80	124	290	Yes	
S30408-ESC	EN 1.4301	A4-80	124	290	No	Beam-to-exterior column joint
S22253-ESC-r	EN 1.4462	10.9	155	565	Yes	

The joint specimens consist of a welded I-shaped column with a cross-section of 300×180×6×10 mm (i.e. outer height H = 300 mm, flange width B = 180 mm, web thickness t_w = 6 mm, flange thickness t_f = 10 mm) and a welded I-shaped beam I-250×150×6×10 mm, the lengths of which are 1800 mm and 1280 mm, respectively. The geometric configuration of the joints, including the bolt spacing, are shown in Fig. 1. The end-plates have a thickness of 10 mm and are welded onto the beam ends and bolted to the column flange using eight M20 bolts in 22 mm clearance holes. The column web is strengthened with two pairs of 10 mm thick continuity plates. For each of the five stiffened end-plate connections, two triangular rib stiffeners are symmetrically placed to reinforce the end-plate, as shown in Fig. 1. The geometric details of an end-plate and corresponding bolt hole layout are presented in Fig. 1 (c).

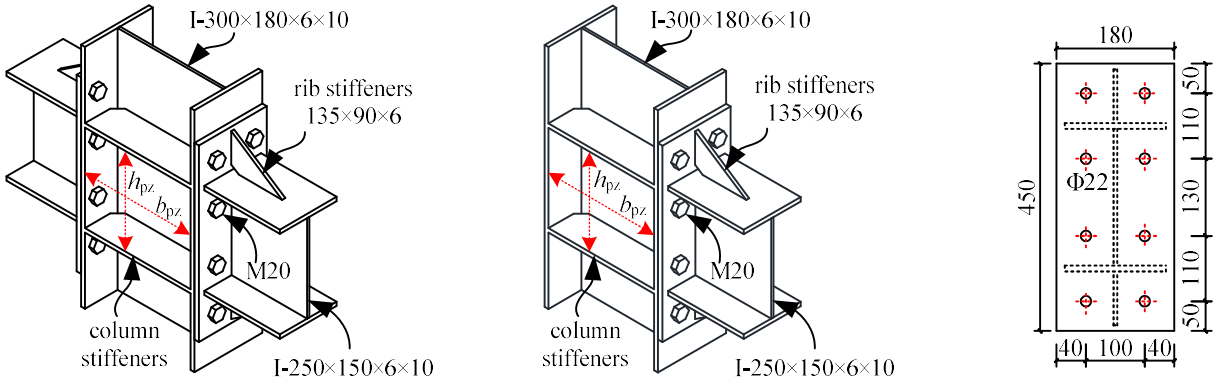

(a) Beam-to-interior column joints (b) Beam-to-exterior column joints (c) Details of end-plate

Fig. 1. Geometric details of joint specimens (all dimensions in mm)

According to both the Chinese standard GB 50011 [30] and the American code ANSI/AISC 341 [31], the dimensions of the panel zone (see Fig. 1 (a) and (b)) should conform to the requirement defined by Eq. (1) to avoid premature shear buckling. The employed panel zone thickness of 6 mm is larger than the minimum required thickness of 5.67 mm defined by Eq. (1) and the corresponding equivalent width-to-thickness ratio λ_{pz} of the panel zone, as defined by Eq. (2), is 85.

$$t_{pz} \geq (h_{pz} + b_{pz})/90 \tag{1}$$

$$\lambda_{pz} = (h_{pz} + b_{pz})/t_{pz} \tag{2}$$

where t_{pz}, h_{pz} and b_{pz} are the thickness, depth and width of the panel zone, respectively (see Fig. 1).

2.2 Material properties of plates and bolts

The material properties of all plates and bolts used in the fabrication of joint specimens were experimentally

determined from standard tensile coupon tests. Flat and round tensile coupons were machined from plate material and bolts taken from the same batch as those employed in the joints and were subsequently tested in tension to failure. The obtained results were reported in detail previously [21], and the average values of key material properties are also summarised in Table 2, including the Young's modulus E_0, the 0.01%, 1.0% and 3.0% proof stresses, the 0.2% proof stress and the corresponding strain $\varepsilon_{0.2}$, the yield stress σ_y and yield strain ε_y of the carbon steel material, the ultimate tensile stress σ_u and the corresponding strain ε_u, and the plastic strain at fracture ε_f. It is noted that two different batches of stainless steel plates with the same nominal thickness were used to build up the columns and the beams, respectively.

Table 2

Measured material properties of stainless steel plates, carbon steel plates, stainless steel bolts and high strength bolts

Material	t or d [a)] (mm)	E_0 (MPa)	$\sigma_{0.01}$ (MPa)	$\sigma_{0.2}(\sigma_y)$ (MPa)	$\varepsilon_{0.2}(\varepsilon_y)$ (%)	$\sigma_{1.0}$ (MPa)	$\sigma_{3.0}$ (MPa)	σ_u (MPa)	ε_u (%)	ε_f (%)
EN 1.4301	5.81	–	185.65	287.59	0.378	322.68	368.11	751.66	56.30	66.78
for column	9.94	179400	177.06	275.94	0.352	319.05	368.01	757.41	53.55	65.49
EN 1.4462	5.89	185500	392.30	538.37	0.476	591.52	636.42	743.86	24.57	39.36
for column	9.82	177800	355.55	555.45	0.501	613.30	656.27	762.11	23.33	37.23
EN 1.4301	5.78	183700	175.87	282.88	0.355	315.17	357.71	755.15	60.45	72.94
for beam	9.78	204200	204.80	296.31	0.346	328.53	372.10	707.33	62.59	70.96
EN1.4462	5.91	196700	394.15	563.79	0.487	598.60	640.18	748.76	26.70	39.82
for beam	9.99	200500	333.64	547.55	0.473	587.50	626.86	739.83	26.24	42.51
Q345B	5.84	213200	–	356.70	0.731	–	–	500.13	16.79	33.42
	9.72	212800	–	410.78	0.851	–	–	537.31	14.27	31.19
Grade A4-80 bolt	10.00	177900	406.05	574.12	0.526	663.45	736.02	746.89	13.95	36.84
Grade 10.9 bolt	10.00	234400	–	1066.26	0.539	–	–	1099.94	3.57	14.32

a) The value of "d" indicates the diameter of the round tensile coupons machined from bolts.

2.3 Test setup and loading protocol

The employed test setup, which was successfully applied previously for the monotonic loading tests [21], is shown in Fig. 2, including the schematic drawing and general view. Both the top and bottom ends of the column were provided with pin-ended boundary conditions using two hinges, whilst the gap between the column top end and the loading frame was filled using a 1400 mm long link column. The compressive force in the columns reported in Table 1 was applied by a hydraulic cylinder at the bottom end of the columns and was kept constant throughout the cyclic loading process. The cyclic load at each beam end was applied using a 600 kN hydraulic actuator. Two hydraulic actuators were needed for the three beam-to-interior column joint specimens (see Fig. 2 (a)), while only one hydraulic actuator was employed for the other three beam-to-exterior column joint (see Fig. 2 (b)). The beam ends were free in the loading direction but were restrained against lateral displacements and torsion by the lateral supports. Both the hydraulic cylinder and the actuators were equipped with the electro-hydraulic servo controlling system, and the attached calibrated load and displacement transducers were able to record the applied forces and corresponding displacement values, respectively.

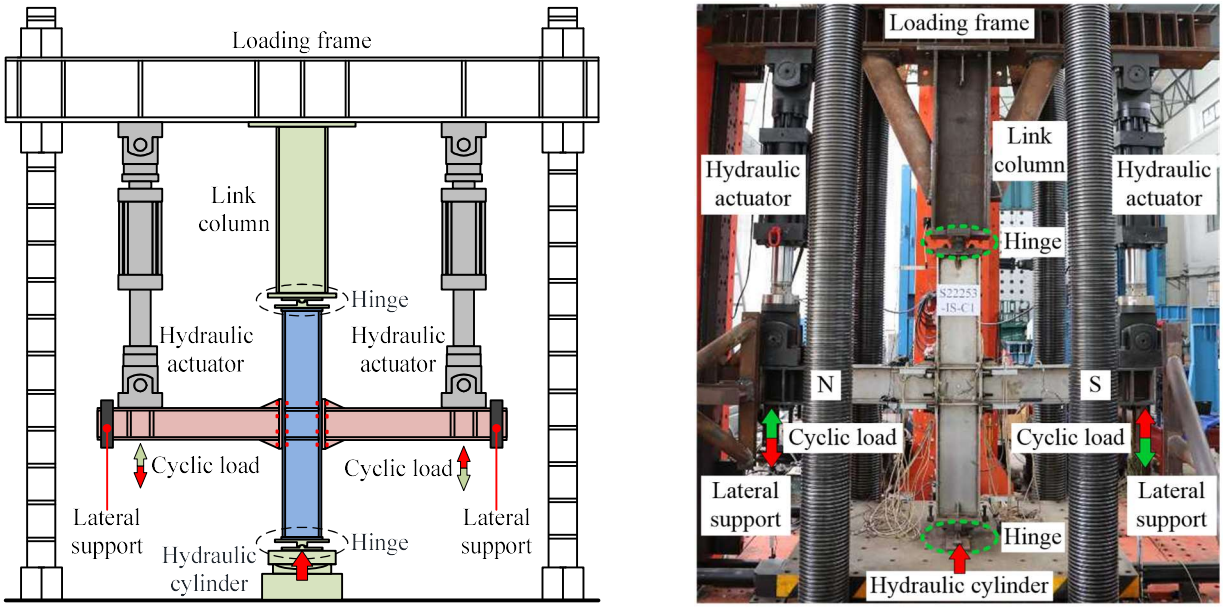

(a) Beam-to-interior column joints

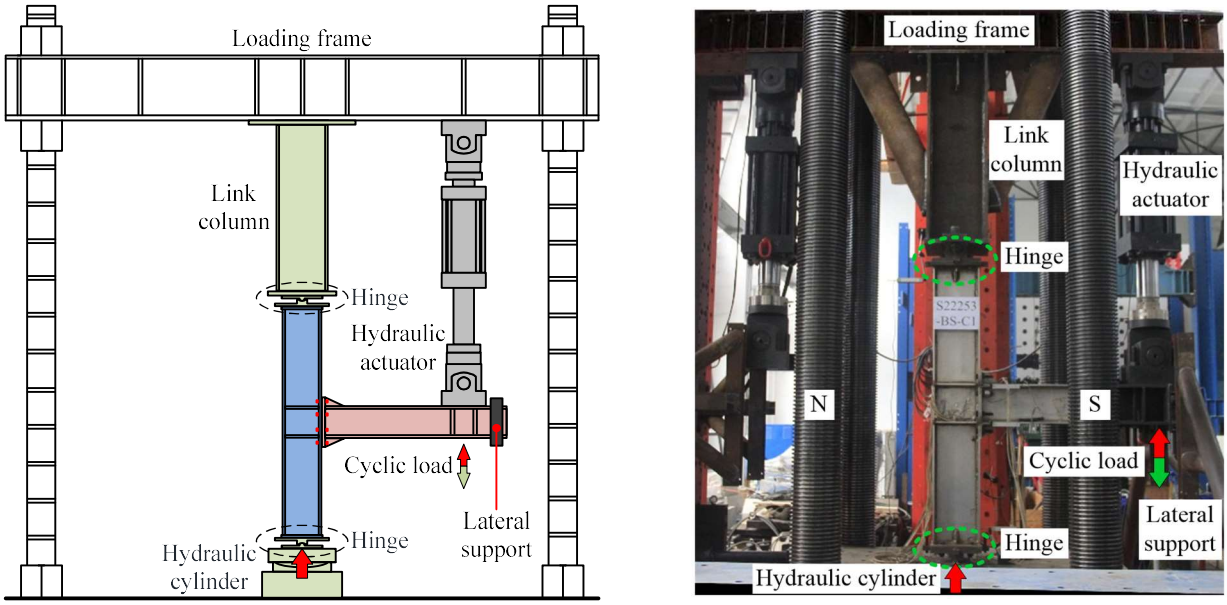

(b) Beam-to-exterior column joints

Fig. 2. Test setup for beam-to-column joint specimens

The loading protocol conformed to the Chinese code JGJ/T 101 [32], as illustrated in Fig. 3. Initially load control is employed for the first three loading cycles until the yield load F_y is reached. Subsequently displacement control is employed starting at the yield displacement Δ_y and increasing step-wise by equal increments of Δ_y. Both the yield load F_y and the corresponding displacement Δ_y have been obtained from the previous monotonic tests [21]. Only one cycle at each step is required during load control, while three repeated cycles at each displacement amplitude are applied. The employed loading rate under load control is 8 kN/min, while the loading rate under displacement control is equal to 3 mm/min until reaching the amplitude of $4\Delta_y$, and then increases to 8 mm/min afterwards. It should be noted that the two beam ends of the beam-to-interior column joints are subjected to antisymmetric loading to simulate the bending moments experienced by a joint in a moment resisting frame during an earthquake. Moreover, the load value and corresponding displacement are marked as positive when the hydraulic actuators move downward, while negative values are assigned for the upward direction.

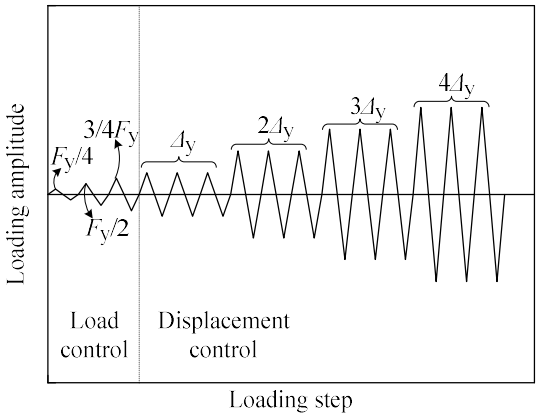

Fig. 3. Loading protocol of cyclic tests

2.4 Instrumentation

Fig. 4 depicts the detailed instrumentation plan for the beam-to-column joint specimens, where a combination of linearly varying displacement transducers (LVDTs), strain gauges and load cells were employed. Four LVDTs were used to record the bending deformations of the two end-plates in the beam-to-interior column joints, as shown in Fig. 4 (a), whilst only two LVDTs in the yellow rectangular box were needed for the beam-to-exterior column joints. Two additional LVDTs were placed along the diagonal lines of each column web panel zone to monitor the shear deformations, as shown in Fig. 4 (b). A total of sixteen uniaxial and five tri-axial strain gauges were adopted to monitor the strain development in key regions of the connections and the panel zone, as shown in Fig. 4 (c). Moreover, four calibrated hollow cylindrical load cells were utilised for each joint specimen to monitor the applied bolt pretension forces and further development of the bolt forces throughout the loading process.

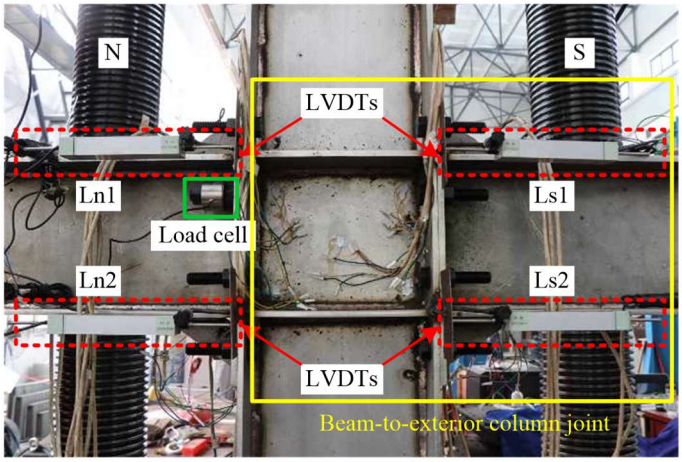

(a) General view

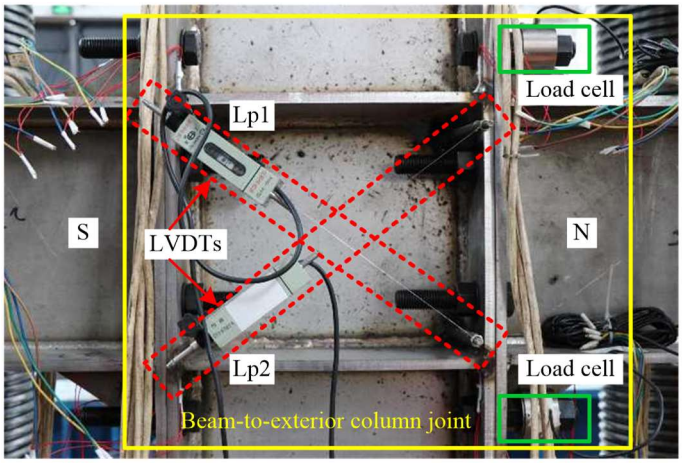

(b) Detailed view of the LVDTs in the panel zone

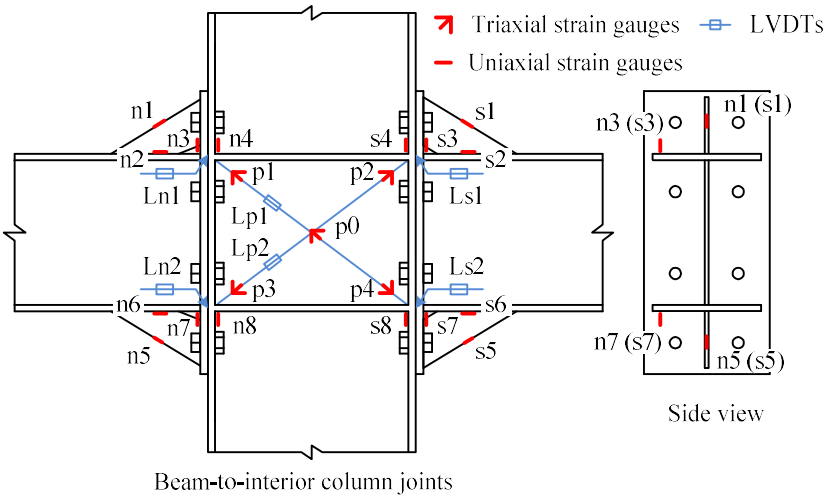

(c) Strain gauges and LVDTs

Fig. 4. Detailed instrumentation plan for beam-to-column joint specimens

3 Cyclic loading test results

3.1 Failure modes

All tested specimens failed by low-cycle fatigue under cyclic loading, with the observed failure modes of the tested joints shown in Fig. 5 and summarised in Table 3, where the number of cycles to failure are also reported. There was no visible local buckling of the beam flanges in any of the tested joints, whilst no bolt fracture was observed. The three beam-to-interior column joints experienced shear buckling of the panel zone and local buckling of the end-plate rib stiffeners, and displayed moderate relative deformation between the end-plate and column flange. The failure of the three beam-to-interior column joints initiated as plastic cracking along the diagonal lines of the column web panel and propagated to severe fracture of the panel zone due to low-cycle fatigue as the number of applied cycles increased. As for the beam-to-exterior column joints, no evident shear buckling in the panel zone was observed, but local buckling of the end-plate rib stiffeners was evident. Moreover, considerable relative deformation between the end-plate and the column flange to which it was bolted developed for the beam-to-exterior column joints, indicating clearly a different failure mechanism to the ones observed for the beam-to-interior column joints. The failure of the two stiffened end-plate exterior column joint specimens was triggered by cracking near the fillet welds between the rib stiffeners and the end-plates, together with the cracking in the welds connecting the end-plates to the beam flanges, while the failure of the unstiffened specimen S30408-ESC was due to low-cycle fatigue fracture in the vicinity of the welds between the end-plate and the upper beam flange. Although fracture occurred in either the panel zone or the welds joining the end-plates, the rib stiffeners to the beam flanges, considerable shear deformation of the panel zone in the beam-to-interior column joints and significant bending deformation of the end-plate in the beam-to-exterior column joints was achieved prior to the fracture as shown in Fig. 5. This ensured sufficient ductility, energy dissipation and inelastic rotational capacity of the tested joints.

Table 3

Failure modes of tested joints

Specimen	Cycles	Failure characteristics
Q345B-ISC-r[a)]	–	Considerable shear deformations and fracture failure of panel zones, local buckling of rib stiffeners, moderate bending deformations of end-plates and column flanges
S30408-ISC-r	27	
S22253-ISC-r	22	
S30408-ESC-r	18	Considerable bending deformations of end-plates and column flanges, local buckling of rib

S30408-ESC	18	stiffeners, fractures located near fillet welds for beam-to-end-plate
S22253-ESC-r	15	

a) The number of cycles for specimen Q345B-ISC-r is not given since this joint experienced undue displacement amplitude in the third cycle owing to accidental miscalculation of test control parameters.

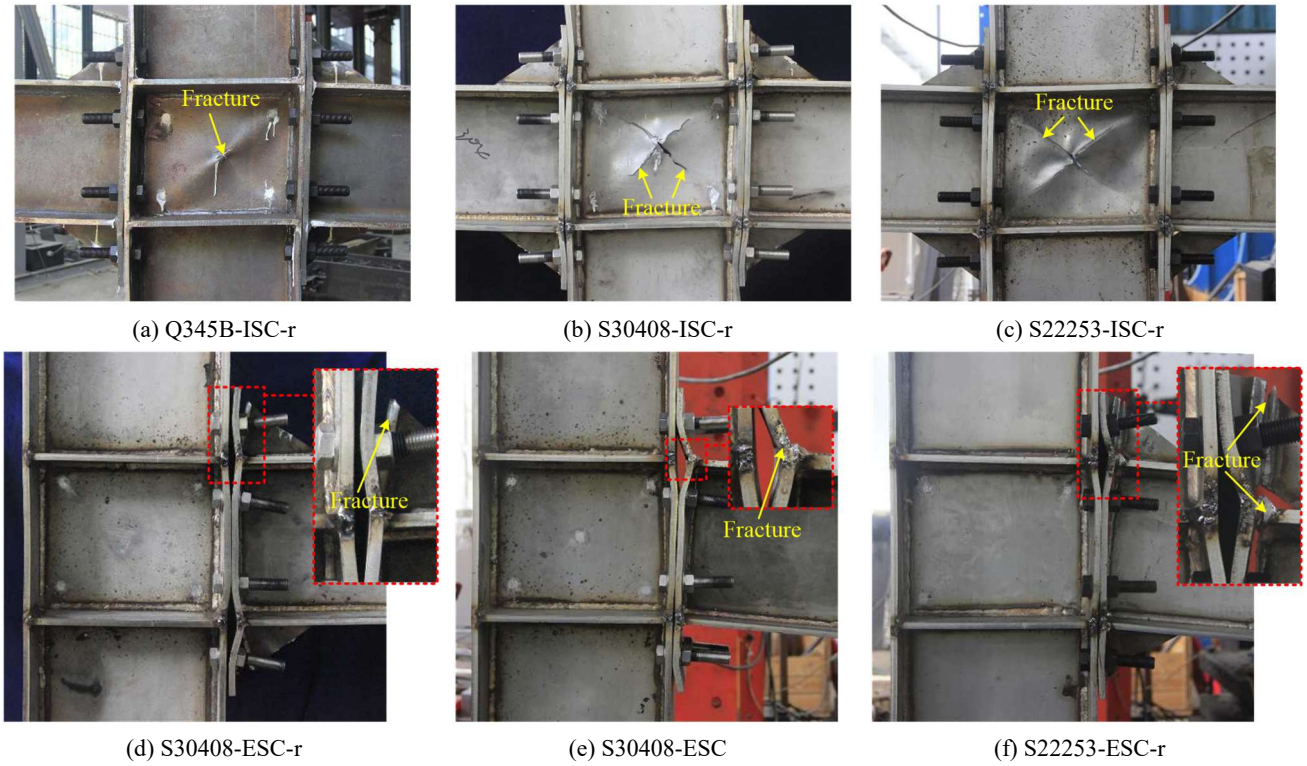

(a) Q345B-ISC-r (b) S30408-ISC-r (c) S22253-ISC-r

(d) S30408-ESC-r (e) S30408-ESC (f) S22253-ESC-r

Fig. 5. Failure modes of tested joints

3.2 Hysteretic curves

The recorded hysteretic response curves of all tested joints are shown in Fig. 6, where the vertical coordinate F is the load applied to the beam end and the horizontal coordinate Δ corresponds to the vertical displacement at the loading point. The symbols 'N' and 'S' were used to mark the responses of the two beams in the north and south directions for the three beam-to-interior column joints, respectively (see Fig. 4). In general, the interior column joints display more stable hysteretic behaviour than their exterior counterparts, the hysteresis curves of which are observed to exhibit mild pinching. The difference in the hysteretic behaviour and associated energy dissipation between the interior and exterior joints can be attributed to differences associated with the failure mode exhibited by each of the two types of joints. As expected [33], failure of the shear panel is highly ductile, whilst for the tested beam-to-exterior column joints, the slippage of bolts between the column flange and the end-plate, plastic cracking near welds of beam-to-end-plate and the developed prying action may generate more considerable stiffness and strength degradation. It is worth mentioning that specimen Q345B-ISC-r experienced accidentally an undue high displacement amplitude in the third cycle owing to a miscalculation of the test control parameters, which resulted in premature and excessive plastic deformations, as indicated by the outmost cycle of the curves in Fig. 6 (a). By comparing the two pairs of specimens – S30408-ISC-r and S22253-ISC-r, and S30408-ESC-r and S22253-ESC-r, it can be seen that more stable hysteretic curves and larger plastic deformations can be achieved by the joint specimens made of the austenitic grade. The introduction of end-plate rib stiffeners contributes significantly to the hysteretic performance of the joints, which is revealed by the fact that the load-carrying capacity and the ductility of the stiffened specimen S30408-ESC-r are much greater than those of the unstiffened counterpart S30408-ESC.

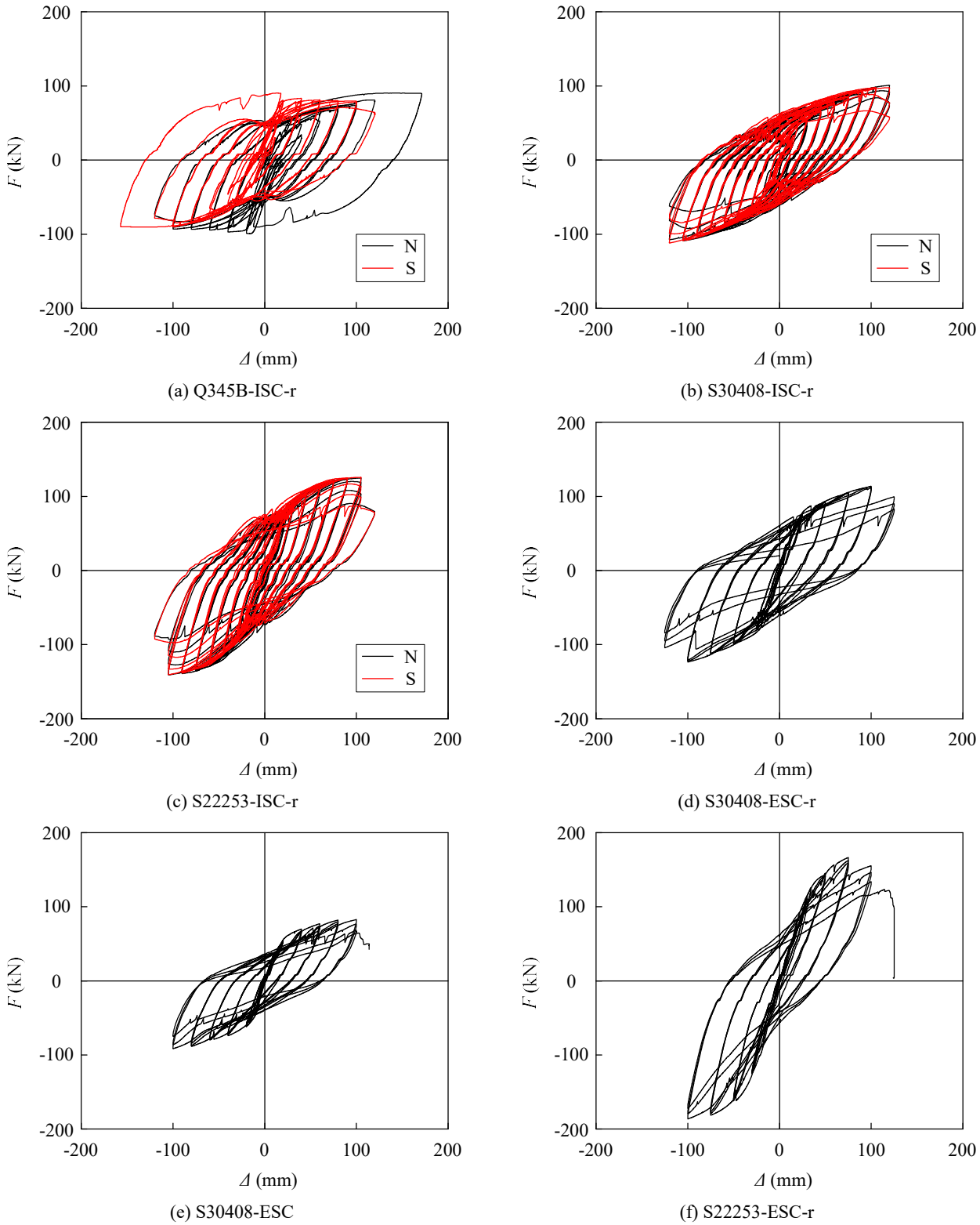

Fig. 6. Hysteresis curves of tested joints

3.3 Skeleton curves and ductility

The envelope curve resulted from connecting the peak points of the first cycle of the hysteresis curves at each loading level is defined as the skeleton curve. The obtained skeleton curves of all tested joints are shown in Fig. 7, where the point symmetric S-shaped skeleton curves indicate that the tested joints experienced a similar amount of degradation of the initial stiffness and the strength in both directions of loading. It is noted that the skeleton curves of the carbon steel joint are distorted by the miscalculation of test control parameters, as previously stated. The obtained skeleton curves of both beams of beam-to-interior column joints agree well with each other, and the skeleton curve of

the stiffened end-plate joint S30408-ESC-r clearly exceeds that of its unstiffened counterpart S30408-ESC.

The comparison between the obtained skeleton curves from the cyclic loading tests and corresponding experimental curves from the monotonic tests reported in [21] is also shown in Fig. 7 for the exterior joint tests. The obtained skeleton curves for the three beam-to-exterior column joints are remarkably close to the respective curves from the monotonic tests up to the attainment of the maximum load, though the initial stiffness of each skeleton curve is slightly lower than that of the corresponding monotonic curve. Subsequently, the envelop curves exhibit significant degradation in strength and ductility due to the considerable damage accumulation associated with increasing number of cycles and displacement amplitudes, whist the monotonic curves are able to sustain additional load. Due to the symmetric loading at the beam ends in the monotonic tests [21], such a comparison is not possible for the interior joint specimens, the loading of which is antisymmetric to induce failure in the panel zone.

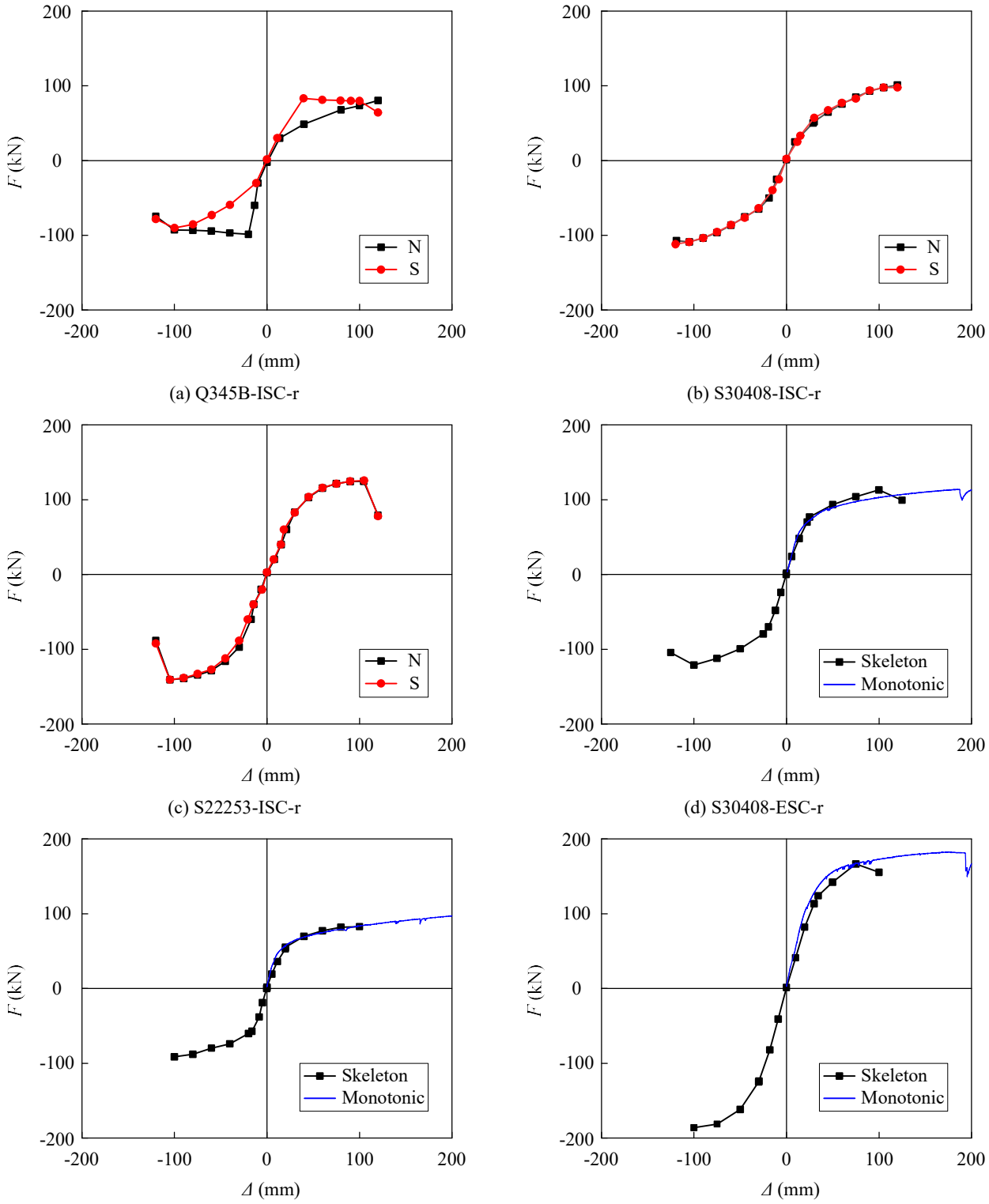

(a) Q345B-ISC-r

(b) S30408-ISC-r

(c) S22253-ISC-r

(d) S30408-ESC-r

(e) S30408-ESC (f) S22253-ESC-r

Fig. 7. Skeleton curves of tested joints

Based on the skeleton curves, the structural properties involving the plastic resistance F_{Rd} as well as the corresponding deformation Δ_{Rd} at the loading point, the maximum resistance F_{max} and the ultimate displacement Δ_u were acquired and are listed in Table 4. The plastic resistance F_{Rd} was taken as the intersection point between the initial stiffness line and the tangent line of the hardening part. The maximum resistance F_{max} was taken as the peak point of the skeleton curve, whilst the ultimate displacement Δ_u corresponded to the maximum displacement of the last loading step. Hence, the plastic moment resistance M_{Rd} and the ultimate moment resistance M_u were computed by simply multiplying the plastic resistance and the ultimate resistance by the lever arm length (equal to 1.1 m), respectively. Furthermore, the initial stiffness K_0 given in Table 4 was determined by linear fitting to the initial loading branches. Similarly, the initial rotation stiffness $S_{j,ini}$ was determined by linear fitting to the initial part of M-φ curves, where the joint rotation capacity φ was acquired by subtracting the elastic beam rotation from the overall rotation at beam end, as described in the previous study [21]. Though there are both positive and negative values for the obtained structural properties due to the cyclic loading history, the average absolute values are presented in Table 4, where the plastic resistance and corresponding plastic deformation of specimen Q345B-ISC-r are not given. It is noted that both the plastic resistance and the ultimate resistance of the beam-to-exterior column joints are higher than their interior counterparts. Furthermore, the presence of rib stiffeners improves the plastic resistance of the joint by approximately 1/3.

The ductility of the beam-to-column joints is defined as the ability to undergo large deformations without pronounced reduction in strength. The ductility coefficient μ is defined as:

$$\mu=\Delta_u/\Delta_{Rd} \quad (3)$$

The calculated coefficient values are shown in Table 4. It can be seen that the beam-to-exterior column joints display greater ductility coefficient values than the beam-to-interior column joints, and the joints made of austenitic grade exhibit greater ductility than those made of duplex grade. In addition, the rib stiffeners have little influence on the ductility by comparing the specimen pair – S30408-ESC-r and S30408-ESC.

Table 4

Experimental results of tested joint specimens

Specimen		F_{Rd} (kN)	F_{max} (kN)	Δ_{Rd} (mm)	Δ_u (mm)	K_0 (kN/mm)	$S_{j,ini}$ (kN·m/rad)	M_{Rd} (kN·m)	M_u (kN·m)	μ	φ_s (rad)	φ_{ep} (rad)	φ (rad)
Q345B-ISC-r	N	–	90.09	–	120.02	–	–	–	99.10	–	–	–	–
	S	–	78.14	–	120.02	–	–	–	85.95	–	–	–	–
S30408-ISC-r	N	62.46	104.12	35.36	119.42	4.82	8547.72	68.71	114.53	3.38	0.083	0.038	0.121
	S	62.33	104.85	33.15	119.91	4.54	7855.95	68.56	115.34	3.62		0.032	0.115
S22253-ISC-r	N	110.52	132.75	45.07	120.06	5.24	9765.41	121.57	146.03	2.66	0.095	0.016	0.111
	S	111.09	133.21	49.06	120.06	5.24	9807.86	122.20	146.53	2.45		0.016	0.111
S30408-ESC-r	S	81.63	117.17	30.71	125.01	5.18	9525.05	89.79	128.89	4.07	0.016	0.102	0.118
S30408-ESC	S	60.91	87.12	24.58	100.03	5.15	9428.95	67.00	95.83	4.07	0.007	0.084	0.091
S22253-ESC-r	S	128.12	176.39	34.58	99.99	6.21	12728.39	140.93	194.03	2.89	0.012	0.067	0.079

4 Analysis of test results

4.1 Bolt force development

The evolution of bolt force throughout the loading process was monitored by four calibrated hollow cylindrical load cells. The degradation of the bolt forces in the tested beam-to-column joints are plotted in Fig. 8, where the

development curves from four stainless steel stiffened end-plate joints are illustrated. The ratio of F_b/F_{pre} can be used to represent the degradation trend of the bolt force, where F_b is the minimum bolt force measured by the calibrated hollow cylindrical load cell at each cycle, and F_{pre} is the initial bolt pretension force. It has to be mentioned that one curve for three joint specimens is absent due to malfunction of one load cell. It can be seen that the bolt force of each bolt row declines with increasing cycles. Moreover, the outer bolt rows (denoted as "1" and "4" in Fig. 8) exhibit earlier and more rapid deterioration than the inner bolt rows (denoted as "2" and "3" in Fig. 8), which can be attributed to the more significant elongation of the bolts in the outer rows, which are subjected to higher tensile forces. In view of the degradation curves of Fig. 8, the exterior column joints display more significant bolt force deterioration in the inner bolt rows than their interior counterparts. This can be explained by the fact that the end-plates of beam-to-exterior column joints experienced much more considerable bending deformation (see Fig. 5).

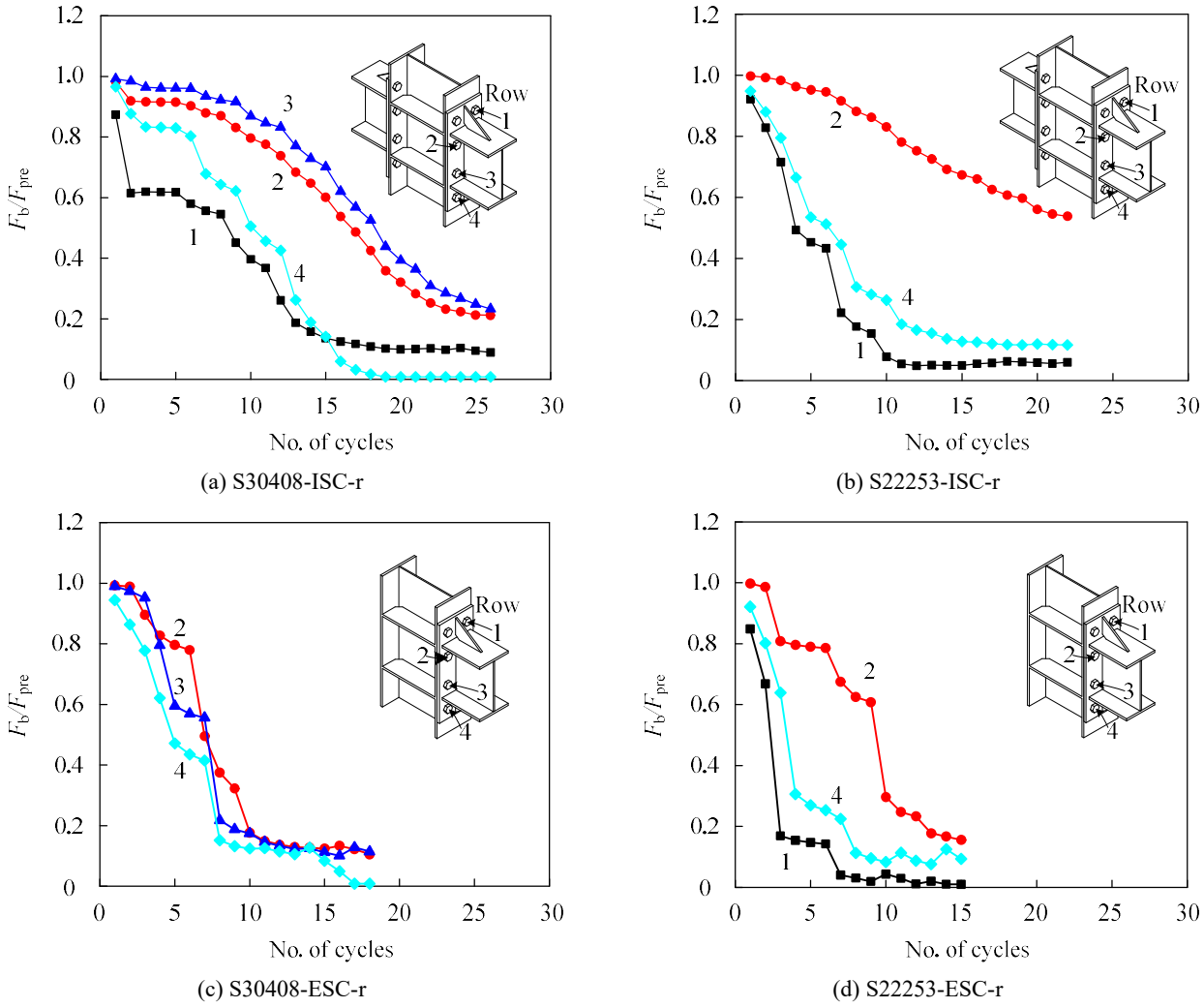

Fig. 8. Bolt force development curves

4.2 Development of strain and deformation in connections

The strain development in the panel zone and the rib stiffeners of two typical stainless steel joints are plotted in Fig. 9, where both tensile (T) and compressive (C) values are included. It is noted that the principle surface strains in the panel zone of the interior column joint S22253-ISC-r are much higher than those of the exterior column joint S22253-ESC-r, and exceed the maximum range of the strain gauges prior to reaching failure. This is associated with the much more considerable shear deformation in the panel zone of the interior column joints illustrated in Fig. 5. Meanwhile, the tensile surface strains in the rib stiffener of the exterior column joint are higher than that of the interior counterpart, while the opposite phenomenon can be observed for the compressive surface strains. This can be explained by the fact that the exterior column joint exhibits more obvious bending deformation in the end-plate, which results in greater

tensile strains in the rib stiffener, while the higher compressive strains in the rib stiffener of the interior column joint are related to the considerable shear deformation of the panel zone.

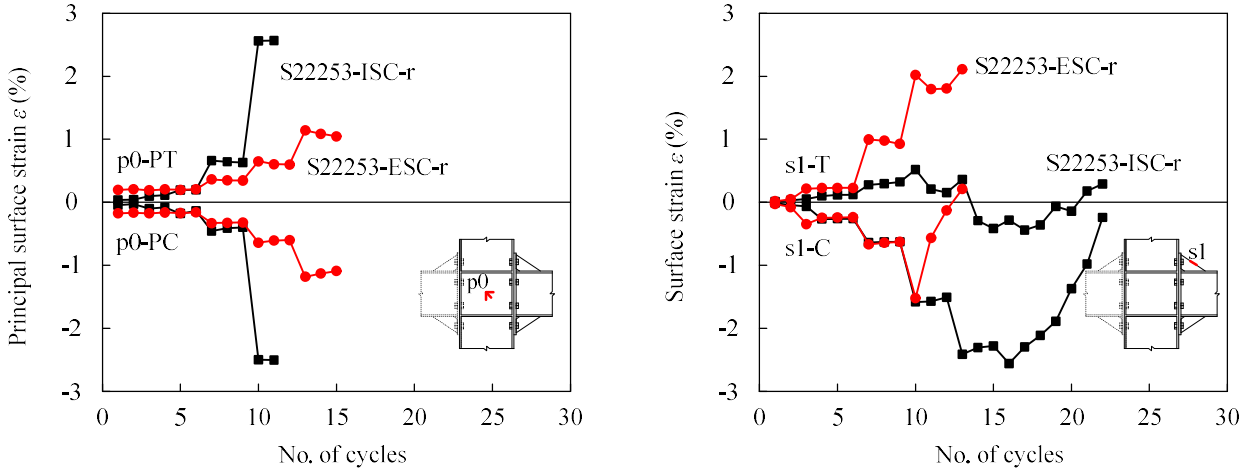

(a) Principle strain development of the panel zone

(b) Strain development of rib stiffeners

Fig. 9. Development of strains in the panel zone and rib stiffeners for duplex stainless steel joints

The evolution of the shear deformation of the panel zone and the separation of the end-plate from the column flange due to the bending deformation of the plates with increasing loading cycles for the same two joint specimens are presented in Fig. 10, where the reported displacement values were partly truncated prior to the maximum deformations due to inadequate recordings from the LVDTs. It can be seen that the shear deformation of the interior column joint is nearly two times that of its exterior counterpart, while the bending deformation in the latter joint is three times as large as that of the first joint.

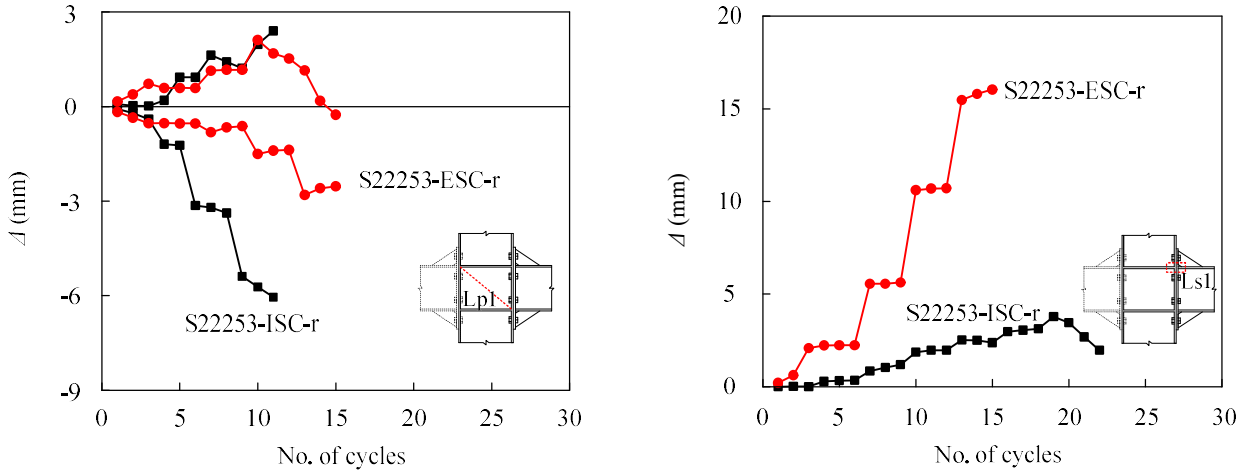

(a) Shear deformation of the panel zone

(b) Gap due to bending deformation between end-plate and column flange

Fig. 10. Deformations of the panel zone and separation of the end-plate from the column flange

4.3 Degradation of stiffness and strength

The ring stiffness K_j at the j-th loading level defined by Eq. (4) [34,35] is generally utilised to evaluate the stiffness deterioration of the tested beam-to-column joints.

$$K_j = \sum_{i=1}^{n} F_{j,i} \Big/ \sum_{i=1}^{n} \Delta_{j,i} \tag{4}$$

where $F_{j,i}$ and $\Delta_{j,i}$ are the peak load and the corresponding displacement of the i-th (i=1, 2, 3) cycle under the j-th loading level, respectively, and n is the number of loading cycles during the j-th loading level. The obtained stiffness degradation curves from the five stainless steel joints are plotted in Fig. 11, where both positive and negative values are depicted for the ring stiffness K_j. It is evident that the ring stiffness K_j decreases significantly with increasing

loading levels, and the degradation of the ring stiffness K_j of the beam-to-exterior column joints is more severe than that of the interior column joints. The joints made of the duplex grade have greater ring stiffness values than their counterparts in austenitic grade, and the presence of rib stiffness is also seen to contribute to the increase of the ring stiffness.

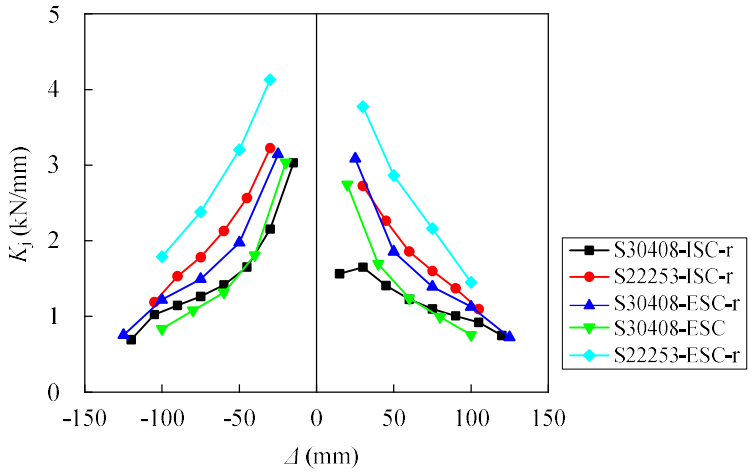

Fig. 11. Stiffness degradation of tested joint specimens

Meanwhile, the strength degradation coefficient λ_i (i=2, 3) defined by Eq. (5) can be used to assess the deterioration of the load-carrying capacity of the tested joints.

$$\lambda_i = \frac{F_{j,i}}{F_{j,1}} \tag{5}$$

where $F_{j,i}$ and $F_{j,1}$ are the peak loads of the i-th cycle and the first cycle at the j-th loading level, respectively. The obtained strength degradation curves are shown in Fig. 12, where the coefficients λ_2 and λ_3 correspond to the second cycle and the third cycle in the same loading level, respectively. It can be seen that no obvious strength degradation has been observed until the last loading level, indicating negligible strength deterioration prior to the failure of the joints. The dramatic decline during the last loading level corresponds to the development of plastic cracking at either the panel zone in beam-to-interior column joints or the welds between end-plate to beam end. As expected, the values of the coefficient λ_3 from the third cycle are lower than the coefficient λ_2 from the second cycle due to the accumulation of damage, and the absence of rib stiffeners can accelerate the strength degradation.

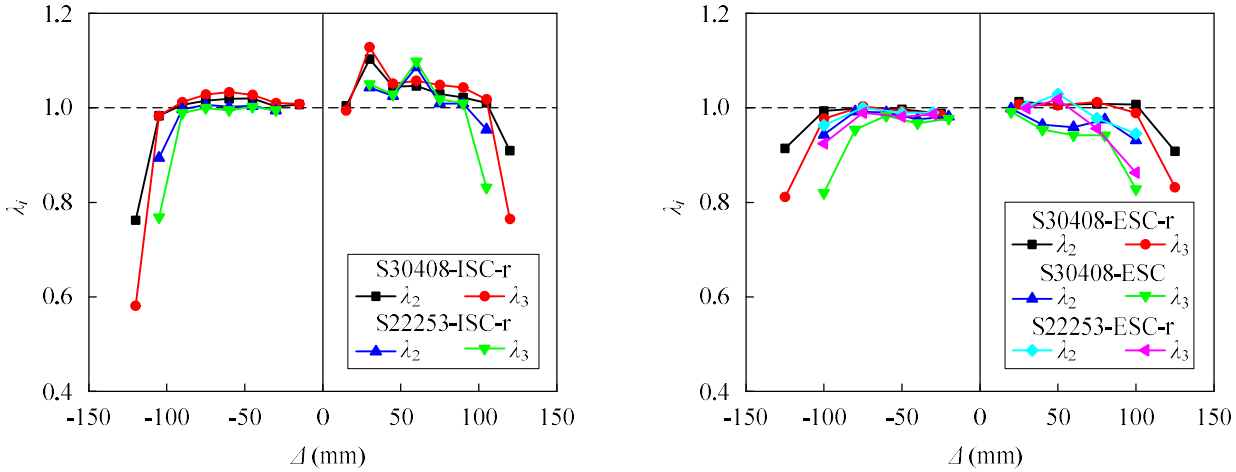

(a) Beam-to-interior column joints

(b) Beam-to-exterior column joints

Fig. 12. Strength degradation curves

4.4 Energy dissipation capacity

The energy dissipation at each load cycle is equal to the area enclosed by the corresponding load-displacement hysteresis loop (see Fig. 13) and can be determined from the recorded hysteretic curves. The cumulatively dissipated

energy W_t that includes all the hysteresis loops, the energy dissipation coefficient E_{ec} and the equivalent viscous damping coefficient ζ_{eq} were therefore calculated for the tested joints and are summarised in Table 5.

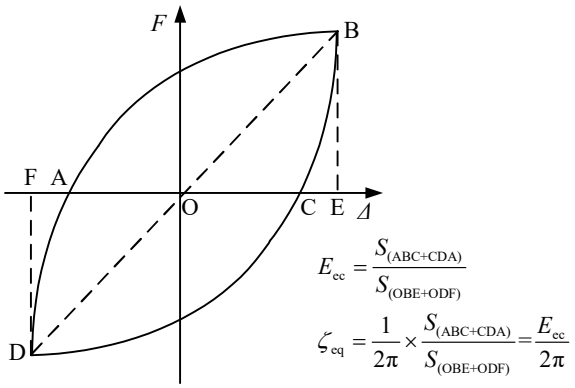

Fig. 13. Load versus displacement hysteresis loop

Table 5

Energy dissipation indices of tested joint specimens

Specimen	$W_{t,test}$ (kJ)		E_{ec}		ζ_{eq}		$W_{t,p}$(kJ)	$W_{t,test}/W_{t,p}$
	N	S	N	S	N	S		
Q345B-ISC-r	120.73	116.19	–	–	–	–	–	–
S30408-ISC-r	230.43	233.05	2.028	2.056	0.323	0.327	185.33	1.25
S22253-ISC-r	218.23	222.53	1.832	1.865	0.292	0.297	195.43	1.13
S30408-ESC-r	–	160.31	–	1.713	–	0.273	143.90	1.11
S30408-ESC	–	83.27	–	1.442	–	0.230	89.33	0.93
S22253-ESC-r	–	107.49	–	1.236	–	0.197	98.71	1.09
Average	–	–	–	–	–	–	–	1.10
St. dev	–	–	–	–	–	–	–	0.11

As shown in Fig. 14 (a), the energy dissipation capacities of the two stainless steel beam-to-interior column joints (S30408-ISC-r and S22253-ISC-r) are roughly equal to two times that of the carbon steel counterpart Q345B-ISC-r. Moreover, the stainless steel beam-to-interior column joints exhibit greater energy dissipation capacities than their exterior counterparts, and the joints made of the austenitic grade demonstrate higher energy dissipation than those made of the duplex grade. This verifies the excellent ductility and energy dissipation associated with failure of the panel zone [33]. The variation of the energy dissipation with increasing load steps for the stainless steel joint specimens in both austenitic and duplex grades are shown in Fig. 14 (b) and (c), where the energy dissipation of south beam in interior column joints are depicted. It is clear that the energy dissipation capacity gradually increases with growing displacement amplitude, and the interior column joints displays much higher dissipation capacities due to the larger amplitude prior to failure. Moreover, the energy dissipation capacity of the first cycle is somewhat higher than the other two cycles, which is in accordance with the strength degradation discussed in the previous sub-section. The specimen S30408-ESC without rib stiffeners has only half the energy dissipation capacity of the stiffened specimen S30408-ESC-r, and this can be noticed from Fig. 14 (a) and (d), which verifies the significant contribution from the presence of end-plate stiffeners.

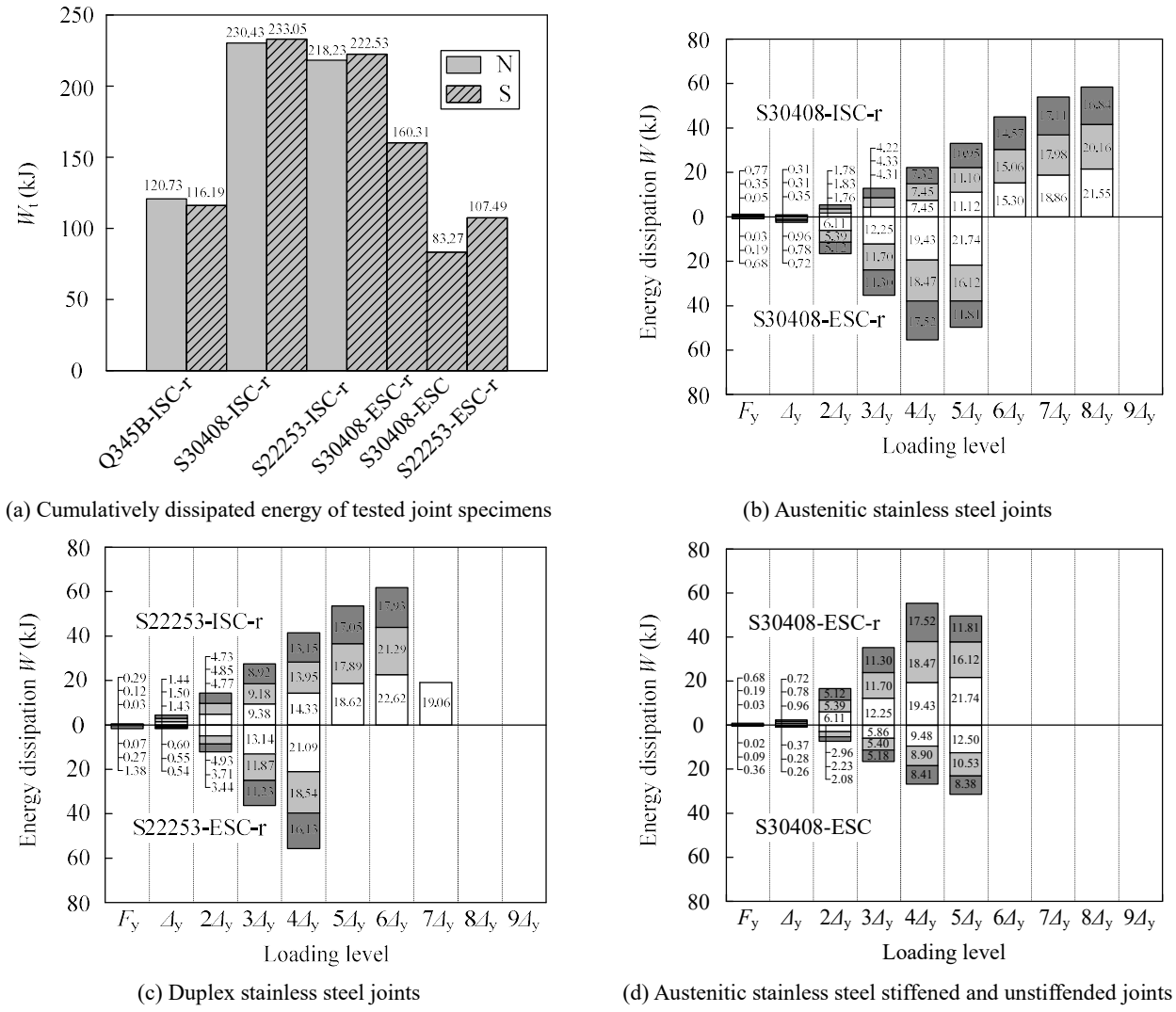

(a) Cumulatively dissipated energy of tested joint specimens

(b) Austenitic stainless steel joints

(c) Duplex stainless steel joints

(d) Austenitic stainless steel stiffened and unstiffended joints

Fig. 14. Cumulatively dissipated energy of tested joint specimens

The energy dissipation coefficient E_{ec} was obtained based on the characteristic at each cycle, and was further utilised to calculate the equivalent viscous damping coefficient ζ_{eq}, as shown in Fig. 13. Hence, these two coefficients exhibit the same pattern, and the development curves of the energy dissipation coefficient E_{ec} for the tested joints are plotted in Fig. 15. The step-wise energy dissipation coefficient values are acquired with increasing loading cycles, during which a slight decline in each loading level can be noticed.

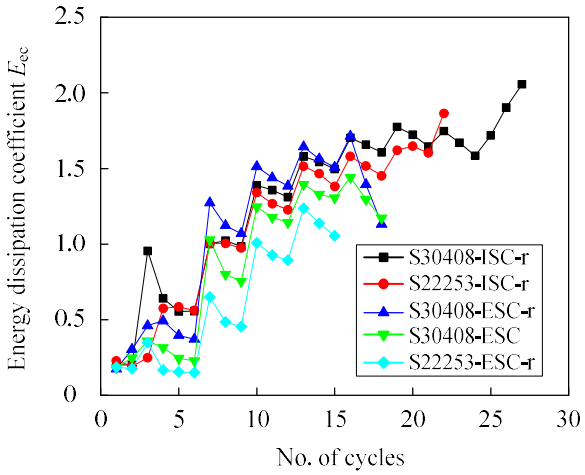

Fig. 15. Development curves of the energy dissipation coefficient

5 Discussion of test results

5.1 Comparison with predictions of empirical hysteresis models

For carbon steel end-plate beam-to-column joints, the bilinear hysteresis model can be utilised to generate hysteretic response curves that were further compared with the obtained test curves [5]. The bilinear peak-pointing hysteresis model proposed by Song et. al. [36] (see Fig. 16 (a)) was employed to approximate the hysteretic curves of stainless steel beam-to-exterior column joints, whilst a trilinear hysteresis model displayed in the Fig. 16 (b) was chosen to approximate the hysteretic curves of stainless steel beam-to-interior column joints in view of the fact that the hysteretic curves of the interior column joints are more stable than those of their exterior counterparts. The initial stiffness K_0 was obtained by linear fitting of the elastic range of the hysteretic curves of the tested joints, as presented in Table 4. The plastic hardening stiffness K_{pl} and the unloading stiffness K_{ul} were determined by introducing two reduction factors r_{pl} and r_{ul}, respectively, which were determined by linear fitting of the part of the curve in the plastic hardening range and unloading range of the F-Δ hysteretic curves respectively, as plotted in Fig. 16 (c) and (d). The average values of the plastic hardening factor r_{pl} and unloading stiffness factor r_{ul} are equal to 0.11 and 0.56, respectively.

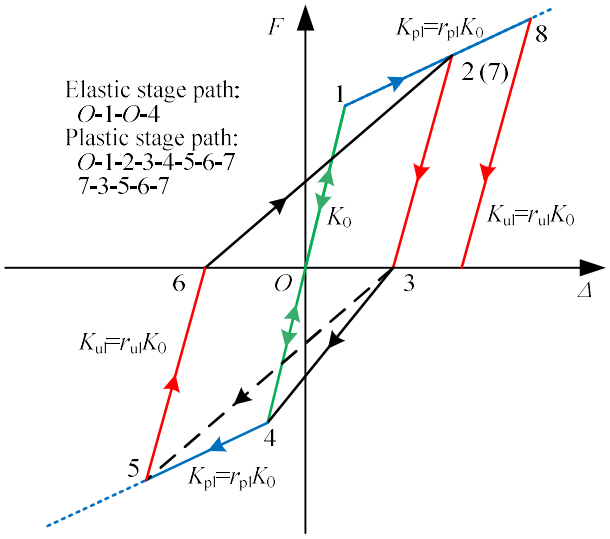

(a) Bilinear peak-pointing hysteresis model

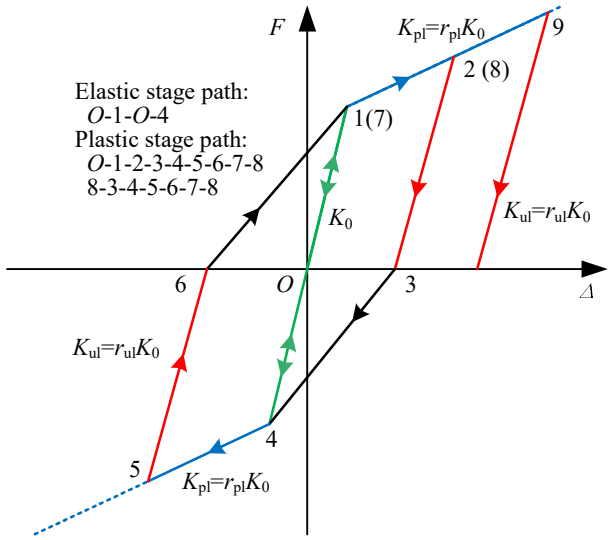

(b) Trilinear hysteresis model

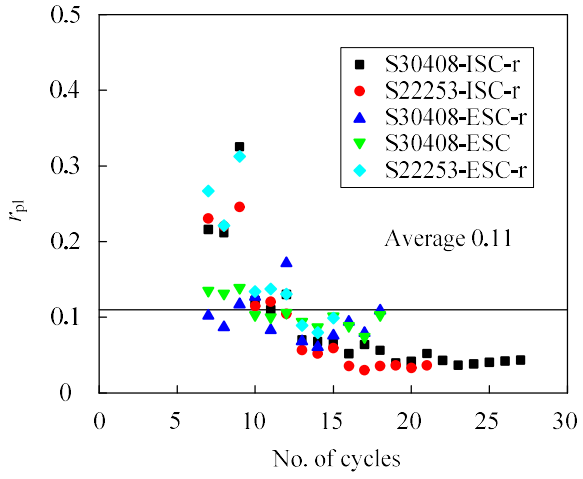

(c) Plastic hardening factor r_{pl}

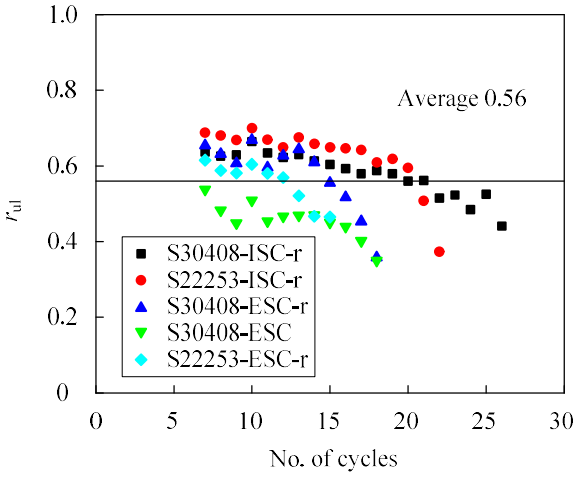

(d) Unloading stiffness factor r_{ul}

Fig. 16. Empirical hysteresis models

The comparison between the analytical curves based on the empirical hysteresis models and the test curves is shown in Fig. 17 for two typical stainless steel joints. It can be seen that the predicted curves are in fair agreement with the test curves until the occurrence of significant stiffness and strength degradation due to cracking initiation and propagation, and hence the mild pinching effect has not been captured. Meanwhile, the predicted cumulatively dissipated energy values are summarised in Table 5, and the average ratio of the test over the predicted energy

dissipation $W_{t,test}/W_{t,p}$ is equal to 1.10 with a standard deviation of 0.11. It can be concluded that the empirical hysteresis models with the coefficients determined by the test curves are able to replicate the hysteretic responses adequately, though the degradation laws of stiffness and strength of the joints are not taken into account.

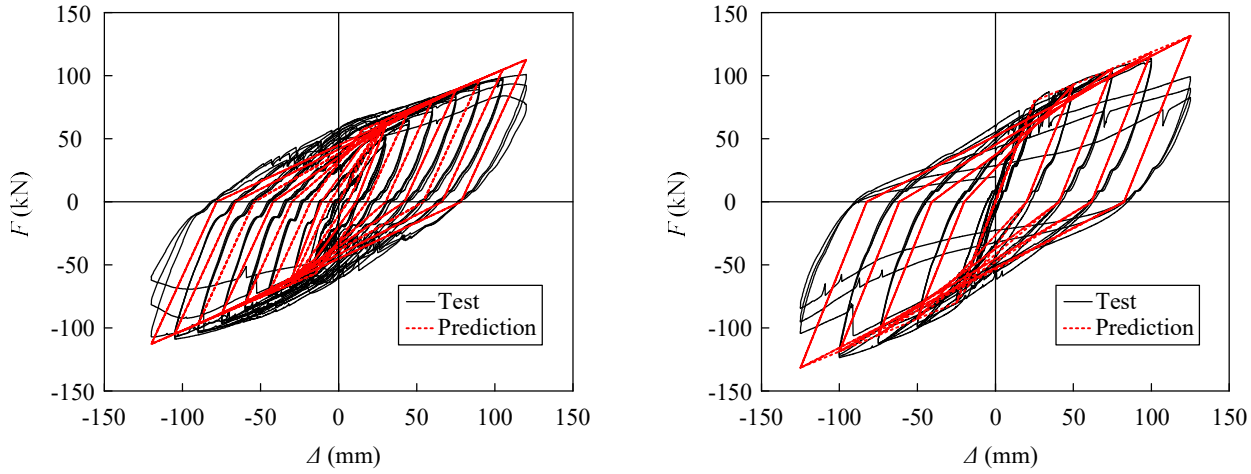

(a) S30408-ISC-r (b) S30408-ESC-r

Fig. 17. Comparison of hysteretic curves

5.2 Comparison with joint rotation capacity in seismic design standards

Explicit limits for the minimum available rotation capacity of beam-to-column joints in earthquake resisting structures are specified in both seismic design standards EN 1998-1 [37] and ANSI/AISC 341 [31]. According to the design provisions in EN 1998-1, the rotation capacity limit values are taken as 0.035 rad and 0.025 rad for structures of ductility class high (DCH) and ductility class medium (DCM), respectively, as design for a higher ductility class allows the use of higher behavioural factors but in turn imposes more onerous ductility demands. Meanwhile, a minimum rotation capacity of 0.03 rad is required by ANSI/AISC 341. In accordance with the requirements of EN 1998-1, the plastic rotation should be ensured under cyclic loading without degradation of strength and stiffness greater than 20%. The rotations resulted from the panel zone shear (φ_s) and the bending deformation between the end-plate and the column flange (φ_{ep}) were separately acquired by the placed LVDTs according to Eqs.(6) and (7). Based on the conducted cyclic loading tests, the calculated joint rotations (φ) and the two components (φ_s and φ_{ep}) are given in Table 4, where average absolute values from both loading directions are presented. It can be seen that the obtained rotation capacities are far in excess of the ductility demands specified in the above two seismic standards, indicating excellent ductility of the tested stainless steel joints.

$$\varphi_s = \frac{\delta_{P1} - \delta_{P2}}{2} \frac{\sqrt{h_{pz}^2 + b_{pz}^2}}{h_{pz} b_{pz}} \tag{6}$$

$$\varphi_{ep} = \frac{\delta_{N1} - \delta_{N2}}{h_t} \quad \text{or} \quad \varphi_{ep} = \frac{\delta_{S1} - \delta_{S2}}{h_t} \tag{7}$$

$$\varphi = \varphi_s + \varphi_{ep} \tag{8}$$

where h_{pz} and b_{pz} are the height and width of the panel zone, respectively, h_t is the distance between the centrelines of top and bottom beam flanges, δ_{P1} and δ_{P2} are the deformation values along the diagonal lines of the web panel, δ_{N1}, δ_{N2}, δ_{S1}, δ_{S2} are the horizontal deformation values between the end-plate and the column flange.

5.3 Assessment of existing design standards

There are no specific provisions for the design of beam-to-column joints under either static or seismic loads in existing design standards for structural stainless steel, and hence the relevant design formulae for carbon steel structures are assessed herein. The calculation formulae for the determination of the plastic moment resistance of joints

in seismic applications are provided in ANSI/AISC 358 [27]. Moreover, the design methods to determine the strength and stiffness of carbon steel end-plate beam-to-column joints under static loads specified in EN 1993-1-8 [26] and GB 51022 [28] are also assessed herein based on the comparison of their predictions against the obtained test results.

The moment resistance of both stiffened and unstiffened end-plated connections with four bolt rows can be determined according to the design procedures codified in ANSI/AISC 358 [27]. The required bolt diameter $d_{b,req}$, the required end-plate thickness $t_{p,req}$ and the column flange thickness t_{cf} for a given moment acting at the face of the column can be determined from Eqs. (9)-(11). Hence the moment resistance that for a given connection configuration (specified bolt diameter, end-plate thickness and column flange thickness) can be calculated as the smallest value of M_f resulting from Eqs. (9)-(11).

$$d_{b,req} = \sqrt{\frac{2M_f}{\pi\phi_n F_{nt}(h_o + h_1)}} \tag{9}$$

$$t_{p,req} = \sqrt{\frac{1.11M_f}{\phi_d F_{yp} Y_p}} \tag{10}$$

$$t_{cf} = \sqrt{\frac{1.11M_f}{\phi_d F_{yc} Y_c}} \tag{11}$$

where M_f is the moment at the face of the column, F_{nt} is the nominal tensile strength of bolt, h_o is the distance from the centreline of the compression flange to the outer bolt row of the tension side, h_1 is the distance from the centreline of the compression flange to the inner bolt row of the tension side, F_{yp} and F_{yc} are specified minimum yield strengths for the end-plate material and the column flange material, respectively, Y_p and Y_c are the yield line mechanism parameters of end-plate and column flange, respectively, and the two resistance factors ϕ_n=0.90 and ϕ_d=1.00. Both these values were set to unity and the nominal yield strengths determined from experiments were used to facilitate a comparison between the code predictions and the test results. It is noted that Eqs. (9)-(11) do not take the panel zone capacity into consideration, and thus they may not be applied to the three beam-to-interior column joints exhibited panel zone failure.

The component method is a semi-analytical method for the design of connections adopted in the European code EN 1993-1-8 [26]. A mechanical model consisting of rigid links and springs that simulate the response of the various idealised components comprising the joint is assumed to reflect the response of the whole joint and the resistance of the joint is assembled based on the resistance of its basic components, for the strength and stiffness of which explicit design equations are provided. The initial rotational stiffness and the moment resistance can be determined from Eqs. (12) and (13), respectively. It is worth mentioning that the approximate value of the transformation parameter β for a double-sided beam-to-column joint under antisymmetric loading is taken as 2, while this value is set to 1 for a single-sided joint.

$$S_{j,ini} = \frac{E_0 z^2}{\mu \sum_i \frac{1}{k_i}}, \quad \mu = 1 \tag{12}$$

$$M_{j,Rd} = \sum_r h_r F_{tr,Rd} \tag{13}$$

where the stiffness ratio μ is equal to 1 for the initial rotational stiffness, k_i is the stiffness coefficient for a basic component i, z is the lever arm, $F_{tr,Rd}$ is the effective design tension resistance of bolt row r, h_r is the distance from bolt row r to the centre of compression, which is assumed to be located at the mid-thickness of the compression flange of the beam.

The calculation formulae for both the moment resistance and the rotational stiffness are provided in GB 51022

[28]. Specifically, the moment resistance of a joint can be determined by the shear strength of the column web panel, as given by Eq. (14), which indicates that the expression can only be applied to the three beam-to-interior column joints experienced panel zone failure. The rotational stiffness of the joint is composed of a combination of the shear stiffness of the column web panel (R_1) and the bending rotational stiffness of the connection (R_2), which can be computed by Eqs. (15)-(17). The bending rotational stiffness of the connection (R_2) is determined by the bending stiffness of the end-plate with a reduction factor 1.1. It is noted that the design provisions in GB 51022 are somewhat similar to those in EN 1993-1-8, where the transformation parameter β is required to be taken into consideration.

$$\frac{M}{d_b d_c t_c} \le f_v \tag{14}$$

$$R = \frac{R_1 R_2}{R_1 + R_2} \tag{15}$$

$$R_1 = G d_b d_c t_p \tag{16}$$

$$R_2 = \frac{6 E_0 I_e h_1^2}{1.1 e_f^3} \tag{17}$$

where M is the summation of bending moments at both beam ends, f_v is the shear strength of the column web panel and is taken as $\sigma_{0.2}/\sqrt{3}$, d_b, d_c and t_c are the height, width and thickness of the column web panel, respectively, G and E_0 are the shear and elastic moduli of the material, respectively, I_e is the second moment of area of the end-plate, h_1 is the distance between the mid-thickness of beam flanges, e_f is the distance between the centre of the tension-side outer bolt row and the outer edge of the rib stiffener.

The predicted initial rotational stiffness values and moment resistances are compared with the experimental ones, as listed in Table 6. The mean values of $S_{j,ini,Exp}/S_{j,ini,EC3}$ and $M_{Rd,Exp}/M_{Rd,EC3}$ ratios are calculated to be 1.12 and 1.14 with corresponding COVs equal to 0.09, indicating slightly conservative predictions for the initial rotational stiffness and the plastic moment resistance; the average value of the experimental to predicted ratios ($M_{Rd,Exp}/M_{Rd,AISC}$) is equal to 1.41 with a COV of 0.15. The observation of the conservative predictions is consistent with the previous studies [11,12,21], and this can be explained by the fact that both the inherent strain hardening characteristics of stainless steels and the strengthening effect of the rib stiffeners in the end-plate compression zone [38,39] have not been explicitly taken into account. Compared to the significant underprediction of the moment resistance of the monotonic static tests [21] by EN 1993-1-8 (average $M_{Rd,Exp}/M_{Rd,EC3}$ of 1.40 [21]), the design provisions in EN 1993-1-8 clearly provide much closer predictions for the moment resistance of joints subject to cyclic loading due to the considerable damage accumulation. For the predictions from the Chinese code GB 51022, the mean ratio of experimental over predicted initial rotational stiffness $S_{j,ini,Exp}/S_{j,ini,GB}$ is 1.84 with a corresponding COV of 0.12. This significant underestimation is due to ignoring the flexibility of two key components – bolt in tension and column flange in bending. The average value of $M_{Rd,Exp}/M_{Rd,GB}$ ratios is equal to 2.08 with a slightly lower COV of 0.03, indicating overly conservative moment resistance predictions. This can be explained by the fact that the strengthen effects of the column stiffener and the column flange on the design shear resistance of the column web panel, as well as the load carrying capacities of three components – end-plate in bending, bolt in tension and column flange in bending, are not taken into account, highlighting that improvements in the predictions of the Chinese code GB 51022 for the panel zone capacity are required.

Table 6

Comparison of experimental results with predicted results from codified methods

Specimen		$S_{j,ini,EC3}$ (kN·m/rad)	$S_{j,ini,GB}$ (kN·m/rad)	$\frac{S_{j,ini,Exp}}{S_{j,ini,EC3}}$	$\frac{S_{j,ini,Exp}}{S_{j,ini,GB}}$	$M_{Rd,AISC}$ (kN·m)	$M_{Rd,EC3}$ (kN·m)	$M_{Rd,GB}$ (kN·m)	$\frac{M_{Rd,Exp}}{M_{Rd,AISC}}$	$\frac{M_{Rd,Exp}}{M_{Rd,EC3}}$	$\frac{M_{Rd,Exp}}{M_{Rd,GB}}$
S30408-ISC-r	N	7090.82	4772.11	1.21	1.79	–	62.88	32.08	–	1.09	2.14
	S	7090.82	4772.11	1.11	1.65	–	62.88	32.08	–	1.09	2.14

S22253-ISC-r	N	8124.44	4955.07	1.20	1.97	–	117.65	60.05	–	1.03	2.02
	S	8124.44	4955.07	1.21	1.98	–	117.65	60.05	–	1.04	2.03
S30408-ESC-r	S	10193.46	6193.07	0.93	1.54	63.62	69.42	–	1.41	1.29	–
S30408-ESC	S	8861.08	–	1.06	–	41.02	52.66	–	1.63	1.27	–
S22253-ESC-r	S	11679.35	6080.86	1.09	2.09	117.55	120.37	–	1.20	1.17	–
Average	–	–	–	1.12	1.84	–	–	–	1.41	1.14	2.08
COV	–	–	–	0.09	0.12	–	–	–	0.15	0.09	0.03

6 Conclusions

The hysteretic performance of stainless steel double extended end-plate beam-to-column joints was experimentally studied in this study. Five full-scale stainless steel joints and one carbon steel benchmark specimen were tested subject to cyclic loading. Analysis of the test results were presented in detail, and were further utilised to verify empirical hysteresis models and assess design formulae applied for carbon steel joints in existing design standards. The following conclusions can be drawn:

(1) The tested stainless steel joints exhibited stable hysteretic curves and favourable ductility, and they displayed much higher energy dissipation capacities than their carbon steel counterpart. Besides, the presence of rib stiffeners on end-plates improved the plastic resistance and the hysteretic performance of the tested joints.

(2) The beam-to-interior column joints developed plastic cracking along the diagonal lines of the column web panel followed by fracture due to low-cycle fatigue, while the beam-to-exterior joints experienced plastic fracture near the fillet welds between the beam and the end-plate. The stainless steel beam-to-interior column joints displayed more stable hysteretic responses and higher energy dissipation capacities than their exterior counterparts, verifying the excellent ductility of the panel zone.

(3) The obtained degradation response of the bolt force, the strain development and the deformation in key regions were in line with the observed failure modes. The tested joints experienced significant stiffness degradation and limited strength deterioration prior to ultimate failure.

(4) The bilinear peak-pointing hysteresis model and the trilinear hysteresis model provided a fairly good approximation with the obtained test results, in terms of the F-Δ hysteresis curves and the energy dissipation capacities, though the degradation of stiffness and strength were not accounted for in the empirical models.

(5) The acquired rotation capacities of the tested stainless steel joints are far in excess of the ductility demands set in current seismic design standards, thus verifying the suitability of the use of stainless steel joints in seismic applications.

(6) The relevant design formulae in the three standards for carbon steel beam-to-column joints – ANSI/AISC 358, EN 1993-1-8 and GB 51022, were all evaluated, and generally conservative predictions were obtained for all the three standards.

Acknowledgements

This study was supported by the Natural Science Foundation of Hubei Province (Grant no. 2018CFB441), National Natural Science Foundation of China (Grant no. 51508424) and the Fundamental Research Funds for the Central Universities (Grant no. 2042017gf0047).

References

[1] FEMA-355D, State of the Art Report on Connection Performance, Washington D.C.: Federal Emergency Management Agency (FEMA), 2000

[2] C. Faella, V. Piluso, G. Rizzano, Structural steel semirigid connections: theory, design and software, CRC press, 2000.
[3] C. Bernuzzi, R. Zandonini, P. Zanon, Experimental analysis and modelling of semi-rigid steel joints under cyclic reversal loading, J. Constr. Steel Res. 38(2) (1996) 95–123.
[4] B. Guo, Q. Gu, F. Liu, Experimental behavior of stiffened and un-stiffened end-plate connections under cyclic loading. J Struct Eng ASCE 132 (9) (2006) 1352–1357.
[5] G. Shi, Y.J. Shi, Y.Q. Wang, Behaviour of end-plate moment connections under earthquake loading, Eng. Struct. 29 (2007) 703–716.
[6] M. Latour, V. Piluso, G. Rizzano, Cyclic modelling of bolted beam-to-column connections: Component approach, J. Earthq. Eng. 15 (2011) 537–563.
[7] S. El-Khoriby, M.A. Sakr, T.M. Khalifa, M.M. Eladly, Modelling and behaviour of beam-to-column connections under axial force and cyclic bending, J. Constr. Steel Res. 129 (2017) 171–184.
[8] H. Augusto, L. Simões da Silva, C. Rebelo, J.M. Castro, Cyclic behaviour characterization of web panel components in bolted end-plate joints, J. Constr. Steel Res. 133 (2017) 310–333.
[9] Y. Song, J. Wang, B. Uy, D. Li, Experimental behaviour and fracture prediction of austenitic stainless steel bolts under combined tension and shear. J. Constr. Steel Res. 166 (2020) 105916.
[10] O. Yapici, M. Theofanous, H.X. Yuan, S. Afshan, S. Dirar, Determination of fracture properties and explicit fracture modelling of stainless steel bolts in tension, Submitted to Engineering Structures for publication in 2020.
[11] M. Elflah, M. Theofanous, S. Dirar, H.X. Yuan, Behaviour of stainless steel beam-to-column joints – Part 1: Experimental investigation, J. Constr. Steel Res. 152 (2019) 183–193.
[12] M. Elflah, M. Theofanous, S. Dirar, Behaviour of stainless steel beam-to-column joints – Part 2: Numerical modelling and parametric study, J. Constr. Steel Res. 152 (2019) 194–212.
[13] M. Elflah, M. Theofanous, S. Dirar, H.X. Yuan, Structural behaviour of stainless steel beam-to-tubular column joints, Eng. Struct. 184 (2019) 158–175.
[14] H.X. Yuan, S. Hu, X.X. Du, L. Yang, X.Y. Cheng, M. Theofanous, Experimental behaviour of stainless steel bolted T-stub connections under monotonic loading, J. Constr. Steel Res. 152 (2019) 213–224.
[15] H.X. Yuan, S. Hu, X.X. Du, L. Yang, X.Y. Cheng, M. Theofanous, Corrigendum to “Experimental behaviour of stainless steel bolted T-stub connections under monotonic loading” [J. Constr. Steel Res. 152 (2019) 213–224], J. Constr. Steel Res. 172 (2020) 105860.
[16] H.X. Yuan, J.D. Gao, M. Theofanous, L. Yang, B.W. Schafer, Initial stiffness and plastic resistance of stainless steel bolted T-stubs in tension. J. Constr. Steel Res. 173 (2020) 106239.
[17] M.J. Hasan, M. Ashraf, B. Uy, Moment-rotation behaviour of top-seat angle bolted connections produced from austenitic stainless steel, J. Constr. Steel Res. 136 (2017) 149–161.
[18] M.J. Hasan, S. Al-Deen, M. Ashraf, Behaviour of top-seat double web angle connection produced from austenitic stainless steel, J. Constr. Steel Res. 155 (2019) 460–479.
[19] M.M. Eladly, Behaviour of stainless steel beam-to-column bolted connections – Part 1: Simplified FE model, J. Constr. Steel Res. 164 (2020) 1–9.
[20] J.D. Gao, H.X. Yuan, X.X. Du, Numerical study on structural behaviour of stainless steel beam-to-column joints with double extended end-plate connections // Ninth International Conference on Advances in Steel Structures (ICASS 2018), Dec 5-7, 2018, Hong Kong, China.
[21] J.D. Gao, H.X. Yuan, X.X. Du, X.B. Hu, M. Theofanous, Structural behaviour of stainless steel double extended end-plate beam-to-column joints under monotonic loading. Thin-Walled Struct. 151 (2020), 106743.
[22] Y.Q. Wang, X.L. Qiao, L.G. Jia, T.X. Zhang, Q.L. Jiang, Experimental research on seismic behavior of stainless steel beam-column connections with different link modes, Journal of Southeast University (Natural Science Edition), 48(2) (2018) 316–322. (in Chinese)
[23] M.M. Liu, G. Shi, Cyclic loading tests of duplex stainless steel beam-to-column joints with WUF-W connections // Ninth International Conference on Advances in Steel Structures (ICASS 2018), Dec 5-7, 2018, Hong Kong, China.
[24] Y. D. Bu, Y. Q. Wang, Y. P. Zhao, Study of stainless steel bolted extended end-plate joints under seismic loading, Thin-Walled Struct. 144 (2019) 1–12.
[25] H.X. Yuan, X.H. Liu, J.L. Liu, M. Theofanous, Experimental behaviour and hysteretic model of austenitic stainless steel bolted T-stubs under cyclic loads, Submitted to Journal of Constructional Steel Research for publication in 2020.
[26] EN 1993-1-8, Eurocode 3: Design of steel structures – Part 1.8: Design of joints, European Standard (CEN), Brussels, Belgium, 2005.
[27] ANSI/AISC 358-16, Prequalified connections for special and intermediate steel moment frames for seismic applications, American Institute of Steel Construction (AISC), Chicago, American, 2016.
[28] GB 51022-2015, Technical code for steel structures of light-weight building with gabled frames, China Architecture & Building Press, Beijing, China, 2015. (in Chinese)
[29] CECS 410:2015, Technical specification for stainless steel structures, China Planning Press, Beijing, 2015. (in Chinese)
[30] GB 50011-2010, Code for seismic design of buildings, China Architecture & Building Press, Beijing, China, 2010. (in Chinese)
[31] ANSI/AISC 341-16, Seismic provisions for structural steel buildings, American Institute of Steel Construction (AISC), Chicago, American, 2016.
[32] JGJ/T 101-2015, Specification for seismic test of buildings, China Architecture & Building Press, Beijing, China, 2015. (in Chinese)
[33] H. Krawinkler, S. Mohasseb. Effects of panel zone deformations on seismic response. J. Constr. Steel Res. 8 (1987) 233–250.
[34] G.F. Du, J. Zhang, Y. Li, J.C. Zhang, L. Zeng, Experimental study on hysteretic model for L-shaped concrete-filled steel tubular column subjected to cyclic loading, Thin-Walled Struct. 144 (2019), 106278.
[35] C.L. Wu, J.M Liu, W.Y. Tan, P.F. Wang, Seismic behavior of composite interior joints of prefabricated H-shaped steel reinforced concrete column - steel beam, Structures, 23(2020), 558–572.
[36] J.K. Song, J. Pincheira, Spectra displacement demands of stiffness and strength degrading systems, Earthq. Spectra, 16(4) (2000) 817–851.
[37] EN 1998-1, Eurocode 8: Design of structures for earthquake resistance – Part 1: General rules, seismic actions and rules for buildings, European Standard (CEN), Brussels, Belgium, 2004.
[38] A. Abidelah, A. Bouchaïr, D.E. Kerdal, Experimental and analytical behavior of bolted end-plate connections with or without stiffeners, J. Constr. Steel Res. 76 (2012) 13–27.
[39] M. D'Aniello, R. Tartaglia, S. Costanzo, R. Landolfo, Seismic design of extended stiffened end-plate joints in the framework of Eurocodes, J. Constr. Steel Res. 128 (2017) 512–527.